ACS OMEGA

Open Access

http://pubs.acs.org/journal/acsodf

Article

FZD7-Targeted Nanoparticles to Enhance Doxorubicin Treatment of Triple-Negative Breast Cancer

Elise C. Hoover, Olivia M. Ruggiero, Rachel N. Swingler, and Emily S. Day*

Cite This: *ACS Omega* 2024, 9, 14323−14335

Read Online

ACCESS | Metrics & More | Article Recommendations | Supporting Information

ABSTRACT: Doxorubicin (DOX) is a chemotherapy agent commonly used to treat triple-negative breast cancer (TNBC), but it has insufficient efficacy against the disease and considerable toxicity due to its off-target delivery. To improve the specificity of DOX for TNBC, we encapsulated it in poly(lactic-*co*-glycolic acid) (PLGA) nanoparticles (NPs) coated with antibodies against Frizzled7 (FZD7), a receptor that is overexpressed on TNBC cells and which is a key activator of the Wnt signaling pathway. In vitro studies show that DOX encapsulation does not hinder its ability to localize to the nucleus in human TNBC cell cultures and that DOX delivered via NPs induces apoptosis and DNA damage via H2A.X phosphorylation to the same degree as freely delivered DOX. FZD7-targeted NPs delivering DOX caused significantly greater inhibition of metabolic activity and led to a smaller cell population following treatment when compared to freely delivered DOX or DOX-loaded NPs coated only with poly(ethylene glycol) (PEG). The FZD7 antibodies additionally provided significant levels of Wnt pathway inhibition, as demonstrated by an increase in β-catenin phosphorylation, indicative of β-catenin destruction and downregulation. These results show that FZD7-targeted platforms have great promise for improving the therapeutic window of otherwise toxic chemotherapies like DOX in TNBC and other cancers that display the overexpression of FZD7 receptors.

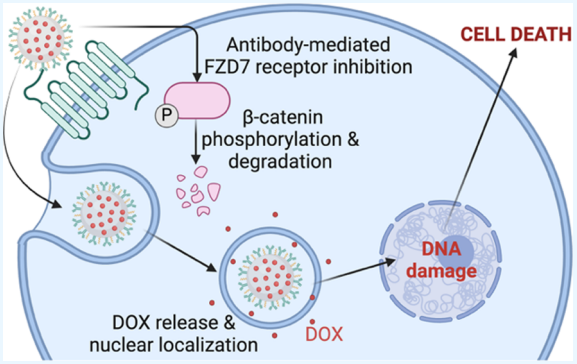

INTRODUCTION

Approximately 1 in 8 women in the United States will develop some form of breast cancer throughout their lifetime.[1] Triple-negative breast cancer (TNBC) accounts for 15−20% of these diagnoses and is associated with a more aggressive disease state and a worse prognosis with a 77% five-year survival rate compared to 93% for non-TNBC breast cancer patients.[2,3] This 5 year survival rate drops to less than 20% in patients with metastatic TNBC.[4] Due to its aggressive nature, TNBC exhibits higher rates of recurrence and metastasis to distant organs than other breast cancer subtypes, making complete eradication of the tumor cells a high priority to prevent further disease progression.[5,6] Due to the lack of expression of human epidermal growth factor receptor 2 (HER2), estrogen receptors, and progesterone receptors, TNBC is unsusceptible to available targeted therapies that leverage these receptors to treat other breast cancer subtypes. The current standard of care for treating TNBC uses nonspecific chemotherapy, debilitating radiation, or invasive surgery, each of which can lead to severe off-target effects and/or insufficient results.[7,8] New treatments are desperately needed to more specifically treat TNBC and improve patient prognoses.

Doxorubicin (DOX) is one of the most common chemotherapeutics used to treat TNBC and is a potent small molecule anthracycline drug.[9,10] Like many other anthracyclines, DOX is an untargeted molecule that, upon systemic delivery, often causes off-target side effects detrimental to the patient such as nausea, vomiting, diarrhea, cardiotoxicity, and bone marrow and subsequent immune suppression.[11,12] Cardiotoxicity in particular is one of the main concerns with the delivery of DOX that restricts its clinical application.[13,14] Due to these dose-limiting side effects that prevent DOX from reaching its full antitumor potential, new delivery mechanisms are being investigated to more adequately and specifically deliver DOX to its intended target. One of the most promising methods to do so is to encapsulate DOX within nanocarriers such as polymer nanoparticles (NPs) or liposomes, as demonstrated with the FDA-approved therapeutic Doxil.[15−17] Here, we aimed to use antibody-modified polymer NPs to specifically deliver DOX to TNBC cells and potentiate its chemotherapeutic effects through the antibody-mediated inhibition of a signaling pathway involved in drug resistance. Polymer NPs were chosen due to their versatility in both cargo loading and surface modifications, allowing for tunable

Received: December 22, 2023
Revised: March 1, 2024
Accepted: March 6, 2024
Published: March 16, 2024

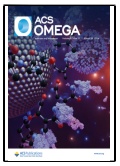

Scheme 1. Depiction of Wnt Signaling Dysregulation in TNBC Cells When Compared to Healthy, Noncancerous Cells[a]

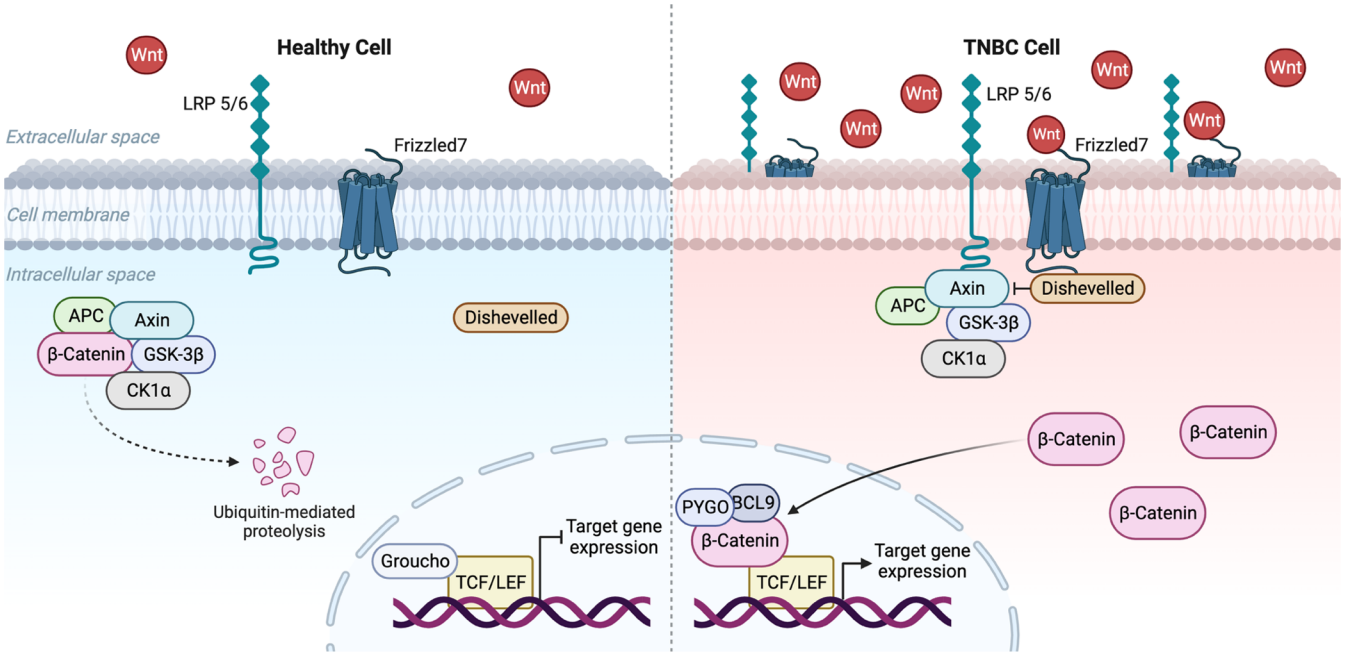

[a]In healthy noncancerous cells, a destruction complex comprised of APC, Axin, GSK-3β, and CK1α degrades β-catenin in the cytoplasm via ubiquitin-mediated proteolysis. This prevents β-catenin movement to the nucleus, therefore leaving downstream Wnt genes off. In TNBC cells, extracellular Wnt ligands bind to overexpressed Frizzled7 (FZD7) receptors, which recruits disheveled to the receptor to inhibit the destruction complex. This allows β-catenin to accumulate in the cytoplasm before translocating to the nucleus to activate the transcription of Wnt target genes that promote oncogenesis. Adapted from "Wnt Signaling Pathway Activation and Inhibition", by BioRender.com (2023). Retrieved from https://app.biorender.com/biorender-templates.

adjustments of targeting and stealthing ligands. Additional advantages of a polymeric NP include minimal cargo leakage and maintenance of structural stability over time, while other NP formulations, including liposome NPs such as Doxil, suffer from drug loss in storage conditions and instabilities in aqueous solutions.[18,19]

In designing our platform, we chose to coat the NPs with antibodies against Frizzled7 (FZD7), a transmembrane receptor that is overexpressed in ~70% of TNBC cases and that plays an important role in the Wnt signaling pathway that has been implicated in many invasive breast cancers including TNBC.[3,20,21] Wnt signaling is typically upregulated during embryonic and fetal development to encourage cell proliferation, migration, and cell fate determination and then transitions to mostly stem cell maintenance in adults.[22−25] Unfortunately, many cancers, including TNBC, have found ways to upregulate the canonical, β-catenin-dependent Wnt pathway in order to promote cell proliferation, migration, and chemoresistance.[26−28] In healthy noncancerous cells, a destruction complex comprised of Axin, APC, GSK-3β, and CK1α continuously degrades cytoplasmic β-catenin to regulate its activity (Scheme 1).[29] In cancer cells that display aberrant Wnt signaling, extracellular Wnt ligands bind to the overexpressed FZD7 receptors, which leads to inhibition of the destruction complex and allows β-catenin to accumulate in the cytoplasm.[30,31] β-catenin then translocates to the nucleus and binds with TCF/LEF to turn on downstream target genes such as Axin2, c-Myc, and cyclin D1 (Scheme 1).[32,33] These genes promote migration, proliferation, drug resistance, and stemness, thus encouraging further tumor growth and disease progression.[34−36] Despite the importance of Wnt signaling in oncogenesis and the wide range of potential targets in this pathway, it has proven challenging to manipulate therapeutically and there are currently no FDA-approved Wnt-targeted therapies on the market.[37,38]

FZD7 is a promising receptor to target for two key reasons. First, its higher levels of expression in TNBC when compared to those in other breast cancer subtypes or healthy tissues make it a useful handle for NP attachment to the cell to improve the precision of DOX delivery.[22,23] Second, NP binding to this receptor can block its activation by extracellular Wnt ligands, thereby suppressing chemoresistance mechanisms that are driven by Wnt signaling and in turn increasing the potency of the delivered DOX.[39−41] As noted above, hyperactive Wnt signaling has been implicated in drug resistance, as it drives the overexpression of drug efflux receptors such as P-glycoprotein/multidrug resistance protein-1 (MDR1) as well as the upregulation of other genes that promote drug resistance including c-Myc and HIF-1α.[42,43] By coating drug-loaded polymer NPs with *anti*-FZD7 antibodies, we aimed to both specifically deliver DOX to TNBC cells and inhibit the Wnt pathway to potentiate DOX's effects. Previously, we showed that FZD7 antibody−NP conjugates based on gold nanoshell cores could bind TNBC cells with greater avidity than freely delivered FZD7 antibodies while also significantly reducing β-catenin protein expression and downstream Axin2 mRNA expression at a much lower antibody dose.[39] This enhanced effect of the NP conjugates can likely be attributed to multivalent binding, wherein antibodies on NPs are able to bind to and inhibit multiple cell surface receptors simultaneously, while freely delivered antibodies can only bind to one receptor at a time.[44−46] Other antibody-conjugated nanocarriers have shown similar success in targeting surface receptors to improve drug delivery and simultaneously

https://doi.org/10.1021/acsomega.3c10275
ACS Omega 2024, 9, 14323−14335

enhance inhibition of downstream signaling.[47−49] Based on this previous work, we developed chemotherapeutic-loaded polymer NPs that also take advantage of multivalent binding to improve the specific targeting and treatment of TNBC.[39,40]

In this work, we demonstrate the synthesis of *anti*-FZD7 antibody-modified NPs that encapsulate DOX and evaluate their effects on MDA-MB-231 human TNBC cells in vitro. We show that DOX encapsulated in NPs maintains its ability to enter the nucleus, damage DNA, and induce apoptosis in TNBC cells and that FZD7-targeted DOX-loaded NPs inhibit cellular metabolic activity to a greater extent than free DOX at concentrations of 5 and 10 μM. Additionally, we demonstrate that FZD7 targeting via antibody-modified NPs successfully triggers β-catenin phosphorylation, indicative of Wnt signaling inhibition. Collectively, these results indicate that loading DOX in FZD7-targeted NPs has promise as a strategy to enhance its delivery to and potency in TNBC cells.

EXPERIMENTAL SECTION

Synthesis of DOX-Loaded NPs. Poly(lactic-*co*-glycolic acid)−poly(ethylene glycol)−maleimide (PLGA−PEG−MAL) NPs containing doxorubicin-HCl (DOX) were synthesized using a double emulsion water-in-oil-in-water method adapted from the literature.[50,51] PLGA−PEG−MAL (20 kDa 50:50 PLGA, 5 kDa PEG, Nanosoft Polymers) was dissolved in dichloromethane (DCM) at 2 mg/mL. Then, 100 μg of DOX (Sigma-Aldrich) dissolved in Milli-Q water was added to a scintillation vial containing 100 μL of 1% poly(vinyl alcohol) (PVA; Sigma-Aldrich) dissolved in water. The quantity of 100 μg DOX per 2 mg of NPs was selected based on the initial analysis of loading capacity and encapsulation efficiency as a function of the amount of DOX added during the first emulsion (Supporting Figure S1). After the DOX was dispersed in 1% PVA, 1 mL of the PLGA−PEG−MAL/DCM solution was added to the same scintillation vial and probe-sonicated on ice with a Fisherbrand model 120 Sonic Dismembrator (Fisher Scientific) at an 80% amplitude for 60 s (10 s on, 5 s off). Next, 3 mL of 0.25% PVA dissolved in phosphate-buffered saline (PBS) was added to the DOX/PLGA−PEG−MAL solution, and the probe was sonicated on ice at an 80% amplitude for 60 s (10 s on, 5 s off). The DCM solvent was allowed to evaporate for 4 h at room temperature under continuous stirring at 800 rpm. Following solvent evaporation, the resulting DOX-loaded NPs were subject to centrifugal filtration to remove excess solvent using Millipore 10 kDa molecular weight cutoff (MWCO) filters (4200*g*, 30 min, 4 °C), then transferred to 2 mL Eppendorf tubes, resuspended in 2 mL of Milli-Q water, and centrifuged for 15 min at 20,000 rcf at 4 °C to pellet the NPs. The supernatant was removed, and the NP pellet was resuspended in 2 mL of fresh Milli-Q water and washed once more by centrifugation before being resuspended a final time in Milli-Q water.

Modification of Antibodies and Conjugation to NPs. To conjugate rabbit antihuman FZD7 antibodies (LS-C383580, LSBio) to the NP surface, the antibodies were first modified to expose free thiols (which can bind exposed maleimide groups on the NPs) and then incubated with the NPs in PBS containing 2 mM ethylenediaminetetraacetic acid (EDTA) overnight on a rocker at 4 °C. To modify the antibodies, they were first incubated with 100× molar excess of tris(2-carboxyethyl) phosphine hydrochloride (TCEP; Sigma-Aldrich) in PBS containing 2 mM EDTA for 1 h at 4 °C on a rocker. Following incubation with TCEP, the antibodies were twice washed in 100 kDa Corning Spin-X UF (Sigma-Aldrich) concentrators for 10 min at 12,000 rcf, 4 °C with PBS to remove excess TCEP. Thereafter, 10 μg of thiol-modified FZD7 antibodies (FZD7-SH) was added per mg of NP for the "low" loading condition and 30 μg of FZD7-SH was added per mg of NP for the "high" loading condition. Following overnight incubation, methoxy-PEG-SH (mPEG-SH; Laysan Bio) was added to the NP/FZD7-SH solution and incubated for 2 h at 4 °C on a rocker. The NP solution was then centrifuged for 15 min at 20,000 rcf at 4 °C to pellet the NPs and remove any unconjugated FZD7-SH or mPEG-SH left in the supernatant. The NP pellet was resuspended in Milli-Q water and washed twice more. Control NPs coated with only mPEG-SH (i.e., PEG−DOX−NPs) were also prepared using the same steps as above but omitting the antibody addition.

Nanoparticle Characterization. A LiteSizer 500 (Anton-Paar) dynamic light scattering (DLS) instrument was used to measure the polydispersity index and ζ-potential of samples diluted in Milli-Q water. A NanoSight NS300 (Malvern Panalytical) nanoparticle tracking analysis system (NTA) was used to measure the NP sample concentration (particles/mL) diluted in Milli-Q water. NP samples were prepared for NTA measurement by diluting a fraction of each sample into 1 mL of Milli-Q water to give a particle count between 20 and 100 particles per frame when introduced to the system. The camera level and focus were adjusted for each sample such that 20% of the visible NPs showed signal saturation, and there were a few "halos" around the NPs. A syringe pump injected the samples at an infusion rate of 50−60 A.U. Three 30 s videos recorded by the NTA were used to calculate NP counts and diameters. The detection threshold was also adjusted so that the blue crosshair count was less than five for each frame. Electron micrographs were obtained using a Zeiss Libra 120 transmission electron microscope (TEM) to visualize the morphology of the nanoparticles. TEM images were obtained with support from the Delaware Bioimaging Center. Samples were prepared in small volumes at equal concentrations on hydrophilic carbon support films with copper grids at 400 mesh, stained with 2% uranyl acetate, and dried prior to imaging.

Antibody loading on the NP surface was quantified using a solution-based enzyme-linked immunosorbent assay (ELISA). Briefly, FZD7-conjugated NPs or NPs coated with only PEG were incubated with 10 μg/mL of horseradish peroxidase (HRP)-conjugated antirabbit IgG (Fisher Scientific) for 1 h at room temperature. Samples were pelleted by centrifugation three times (20,000 rcf, 15 min) to remove unbound secondary antibodies in the supernatant and then suspended in 3% bovine serum albumin in PBS. Samples were developed in 3,3′,5,5′-tetramethylbenzidine (TMB, Sigma-Aldrich) core for 1 min before adding 2 M sulfuric acid to stop the reaction. Absorbance at 450 nm was measured on a Synergy H1 plate reader (BioTek) and compared to a standard curve of known HRP-*anti*-IgG concentration to calculate the number of FZD7 antibodies per NP. The number of NPs per sample was obtained by using NTA.

The surface coverage of NPs was calculated by dividing the total antibody area by the NP surface area. The cross-sectional area of the antibody was assumed to be ∼60 nm^2 due to the width of the antibody across the Fab region being ∼15 nm and the width of the Fc region being ∼4 nm. The total number of antibodies loaded on the surface was multiplied by the antibody cross-sectional area to calculate the total antibody

https://doi.org/10.1021/acsomega.3c10275
ACS Omega 2024, 9, 14323−14335

surface area, while the bare NP surface area was calculated using SA = $4\pi r^2$.

Quantification of available maleimide binding sites on the NP surface was performed by using a Colorimetric Maleimide Assay Kit (Sigma-Aldrich). Briefly, an excess of free thiols in the form of 1× MEA (2-aminoethanethiol hydrochloride) was added either to a control buffer solution (provided in the kit) or to 0.05 mg of bare NPs suspended in the buffer solution. The remaining free thiols that did not react with the maleimide were quantified after adding 1× of 4,4′-dithiodipyridine to the solution by reading the absorbance at 324 nm on a Synergy H1 plate reader. The amount of maleimide was calculated as the difference between the initial amount of free thiol and the amount of unreacted thiol following incubation with the maleimide−NPs.

DOX Encapsulation Efficiency, Loading Capacity, and Drug Release of NPs. To calculate DOX encapsulation and loading capacity in the PLGA NPs, 500 μL of dimethyl sulfoxide (DMSO; VWR) was added to 0.5 mg of NPs in a 1.5 mL Eppendorf tube. The tubes were then vortexed for 1 min. The NP/DMSO solution was added to a 96-well plate in triplicate 100 μL volumes. A standard curve of known DOX concentration serially diluted in DMSO was also plated in 100 μL volumes. The fluorescence of the samples and standard curve were read at 480 nm excitation/590 nm emission on a Synergy H1 plate reader. The encapsulation efficiency (EE%) was calculated as $\text{EE\%} = \frac{\text{mass of DOX encapsulated in NPs}}{\text{mass of DOX added to NP synthesis}} \times 100$. The loading capacity (LC, μg DOX/mg PLGA) was calculated as $\text{LC} = \frac{\text{mass of DOX encapsulated in NPs}}{\text{total NP mass}}$.

Drug release was measured by adding 0.5 mg of NPs to 1 mL of either a storage condition (pH 7.4 Milli-Q water, 4 °C) or a tumor microenvironment condition (pH 5.5 PBS, 37 °C shaking at 100 rpm). At each time point (1, 2, 4, 18, 24 h), the sample was centrifuged for 15 min at 20,000 rcf and the supernatant was collected. The supernatant was read in 100 μL volumes on a plate reader and compared to a known standard curve of DOX suspended under each condition. These experiments were performed in triplicate.

NP diameter stability in serum was measured by suspending 0.5 mg of NPs in 1 mL of 10% fetal bovine serum (FBS) in pH 7.4 PBS (Supporting Figure S2). The NP solution was incubated at 37 °C while shaking at 60 rpm. Samples from the solution were collected at each time point (24, 48, 72 h), and the mode diameter was recorded using NTA.

Cell Culture. MDA-MB-231 human TNBC cells (American Type Culture Collection, ATCC) were cultured in Dulbecco's modified Eagle's medium (DMEM; Fisher Scientific) supplemented with 10% fetal bovine serum (FBS; Gemini Bio Products) and 1% penicillin−streptomycin (pen-strep; VWR). Cells were cultured in T75 cell culture flasks at 37 °C in a 5% CO_2 environment. Cells were passaged or plated when they reached 80−90% confluency and were detached from the flask using 3 mL of 0.25% trypsin−EDTA (ThermoFisher). Cells were counted using a hemocytometer.

Imaging of Nuclear Uptake of DOX. To assess DOX uptake and colocalization with the nucleus, 3×10^4 MDA-MB-231 cells were seeded per well of an 8-well chamber plate in DMEM media and incubated overnight. Cells were then treated with free DOX, PEG−DOX−NPs, low FZD7−DOX−NPs, or high FZD7−DOX−NPs at 5 μM. After either 4 or 24 h of treatment, cells were washed twice with PBS to remove media and excess/noninternalized DOX. Cells were fixed with 4% formaldehyde for 15 min and then washed twice with PBS. Following fixation, cells were permeabilized with 0.5% Triton-X in 5% PBSA for 10 min and then washed twice with PBS. Once the cells were fixed, the chamber walls were removed and a glass coverslip was sealed onto the slide using VectaShield AntiFade Mounting Medium with DAPI (Vector Laboratories). Samples were incubated with DAPI for at least 30 min before imaging. Images were acquired at 20× magnification on a Zeiss Axioobserver Z1 inverted fluorescence microscope (DAPI: 365 nm excitation/465 nm emission; DOX: 470 nm excitation/552 nm emission).

DOX fluorescence in the images was analyzed using ImageJ (see Supporting Figures S3 and S4). Briefly, the DAPI-stained nuclei were used to outline and define the regions of interest (ROIs) in each image. Five background values selected randomly were captured for each image to account for the background signal. Once the ROIs were defined, the area, integrated density, and mean gray value for each ROI were measured, and the corrected total nuclear fluorescence (CTNF) was calculated using the following formula

$$\text{CTNF} = \text{integrated density} - (\text{area of selected cell} \times \text{mean fluorescence of background})$$

Evaluating DNA Damage Induced by Free DOX or NPs. To examine the mechanism of cell death induced through DOX delivery, the phosphorylation of H2A.X at serine 139 was quantified using a H2A.X Phosphorylation Assay Flow Cytometry Kit (Sigma-Aldrich). For this assay, 5×10^5 MDA-MB-231 cells were seeded per well of a 12-well plate in DMEM media and incubated overnight. Cells were then treated with free DOX, PEG−DOX−NPs, low FZD7−DOX−NPs, or high FZD7−DOX−NPs at 5 μM for 24 h. Then, cells were washed with PBS before adding trypsin−EDTA to detach the cells. The cells were washed with PBS by spinning them down for 5 min at 300 rcf and 21 °C. Cells were then fixed, permeabilized, and incubated for 20 min in the dark with either FITC-conjugated antiphospho H2A.X or normal mouse IgG antibodies provided in the kit per the manufacturer's instructions. Cell samples were washed twice with Wash Solution provided by the manufacturer to remove any unbound antibodies and were resuspended in PBS. Samples were analyzed immediately using flow cytometry. An Acea NovoCyte 2060 Flow Cytometer was used to analyze the FITC channel (488 nm excitation/530 nm emission). Data analysis was performed with NovoExpress software (ACEA Biosciences). Density plots showing forward and side scatter data were used to create a primary gate for cells, excluding debris. These experiments were performed in triplicate and analyzed by a one-way analysis of variance (ANOVA).

Assessment of Cellular Metabolic Activity. To evaluate the effects of freely delivered DOX versus DOX encapsulated in NPs on cellular metabolic activity, an MTT (3-(4,5-dimethylthiazol-2-yl)-2,5-diphenyltetrazolium bromide) assay (ThermoFisher) was used. MDA-MB-231 cells were plated in a 96-well plate at 5×10^3 cells per well and incubated overnight. Cells were then treated with free DOX, PEG−DOX−NPs, Low FZD7−DOX−NPs, or High FZD7−DOX−NPs at either 2.5, 5, or 10 μM DOX for 24 h. Free DOX effect on metabolic activity was assessed from 0.5 to 20 μM to determine the treatment range for NP experiments (Supporting Figure S5). After 24 h, the treatments were removed and

https://doi.org/10.1021/acsomega.3c10275
ACS Omega 2024, 9, 14323−14335

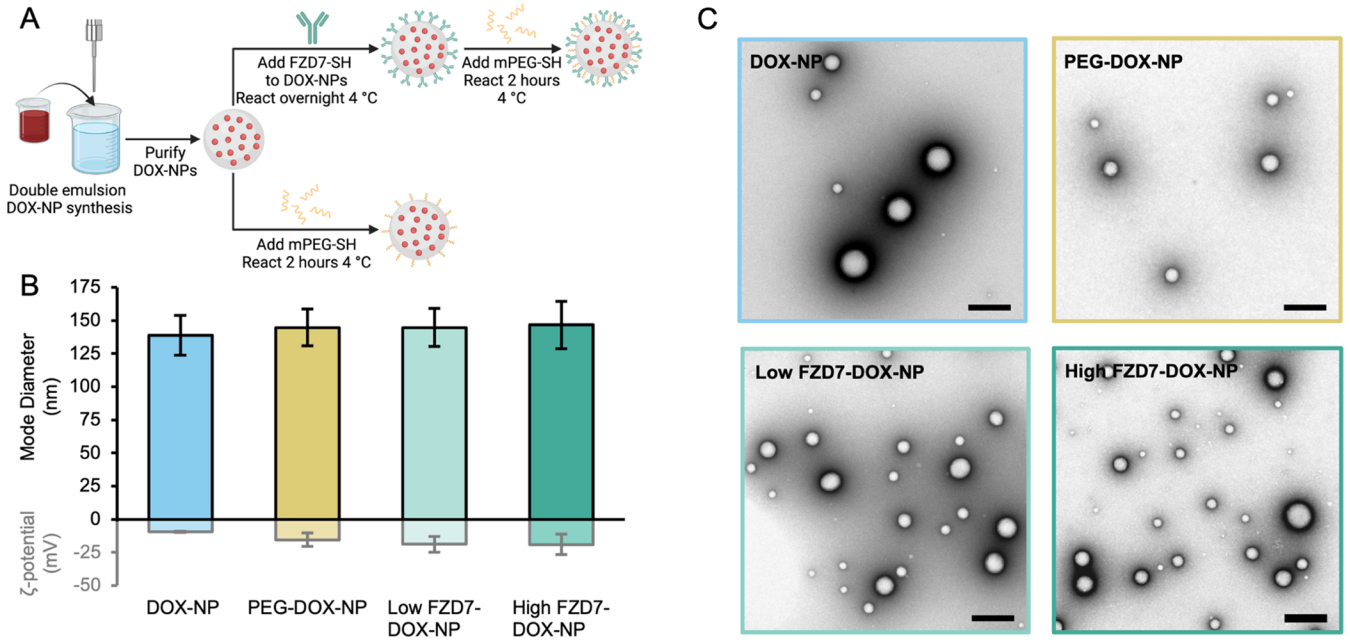

Figure 1. Characterization of NPs. (A) Abbreviated scheme depicting the synthesis of DOX-loaded, surface-modified NPs. Created with BioRender.com. (B) NTA mode diameter and ζ-potential of unmodified (bare) DOX−NPs (n = 6), PEG−DOX−NPs (n = 10), low FZD7−DOX−NPs (n = 10), and high FZD7−DOX−NPs (n = 10). (C) Transmission electron micrographs of unmodified DOX−NPs, PEG−DOX−NPs, low FZD7−DOX−NPs, and high FZD7−DOX−NPs. Scale bars: 200 nm.

12 mM MTT solution was added to the cells per the manufacturer's instructions. After 3 h, the MTT solution was replaced with DMSO and the absorbance read at 540 nm on a Synergy H1 plate reader. Samples were plated in triplicate and normalized to untreated cells. The MTT assay was also performed using empty NPs at 4, 10, 20, and 40 μM dosages based on matching the number of empty NPs to the corresponding number of DOX-loaded NPs (Supporting Figure S5). These experiments were performed in at least triplicate and analyzed by one-way ANOVA with post hoc Tukey.

Quantification of Cell Count. To assess the effects of freely delivered DOX versus DOX encapsulated in NPs on the overall cell viability, cells were counted after treatment with 5 μM free DOX, PEG−DOX−NPs, low FZD7−DOX−NPs, or high FZD7−DOX−NPs for 18 h and compared to untreated cells. MDA-MB-231 cells were plated in a 48-well plate and incubated overnight before the addition of treatments. Following the 18 h treatment, the media/treatments were removed, and the cells were washed twice with PBS before the addition of trypsin−EDTA to detach the cells. The cells were then washed with PBS by centrifuging for 5 min at 300 rcf and 21 °C followed by a wash with flow cytometry buffer using the same settings. The supernatants were discarded, and 150 μL of flow cytometry buffer (ThermoFisher) was then added before analyzing samples using flow cytometry. An Acea NovoCyte 2060 Flow Cytometer was used to analyze the samples. Data analysis was performed with NovoExpress software. Density plots showing forward and side scatter data were used to create a primary gate for cells, excluding debris, and final cell counts within the primary gate were recorded. These experiments were performed in at least triplicate and analyzed by one-way ANOVA with post hoc Tukey.

Evaluating Cellular Apoptosis or Necrosis. To assess the effects of DOX on cell apoptosis, 3×10^5 MDA-MB-231 cells were seeded per well of a 48-well plate in DMEM media and incubated overnight. Cells were then treated with free DOX, PEG−DOX−NPs, low FZD7−DOX−NPs, or high FZD7−DOX−NPs at 5 μM for 18 h. After 18 h, the cells were stained with Annexin V (ThermoFisher) and SYTOX AADvanced Dead Cell Stain (ThermoFisher) per the manufacturer's instructions. In short, the media/treatments were removed, and the cells were washed twice with PBS before adding trypsin−EDTA to detach the cells. The cells were then washed with PBS by centrifuging for 5 min at 300 rcf and 21 °C followed by a wash with 1× binding buffer (ThermoFisher) using the same settings. The supernatants were discarded, and the cell pellets were resuspended in 50 μL of Annexin V FITC/SYTOX AADvanced staining solution containing 1:500 Annexin V and 1:1600 SYTOX. Samples were then incubated in the dark for 15 min at room temperature. An additional 150 μL of 1× binding buffer was then added before analyzing samples using flow cytometry. An Acea NovoCyte 2060 Flow Cytometer was used to analyze samples with FITC (Annexin V), APC (SYTOX AADvanced), and PE (DOX) channels. Data analysis was performed with NovoExpress software. Density plots showing forward and side scatter data were used to create a primary gate for cells, excluding debris, prior to establishing gates for Annexin V-positive and SYTOX AADvanced-positive cells. Positively stained gates were based on unstained cells, and single-stained controls were used for compensation. These experiments were performed in at least triplicate and analyzed by one-way ANOVA with post hoc Tukey.

Live/Dead Stain. To assess the effects of DOX on cell death, 3×10^5 MDA-MB-231 cells were seeded per well of a 48-well plate in DMEM media and incubated overnight. Cells were then treated with free DOX, PEG−DOX−NPs, low FZD7−DOX−NPs, or high FZD7−DOX−NPs at 5 μM for 24 h. After 24 h, the cells were stained using a Live/Dead Viability/Cytotoxicity kit (ThermoFisher) per the manufacturer's instructions. In short, the media/treatments were

https://doi.org/10.1021/acsomega.3c10275
ACS Omega 2024, 9, 14323−14335

removed, and the cells were washed twice with PBS before adding 100 μL of staining solution containing 1:500 ethidium homodimer-1 and 1:2000 calcein-AM. Samples were incubated in the dark for 30 min at room temperature. The staining solution was then removed, and the cells were washed twice with PBS. Images were acquired at 20× magnification on an EVOS M5000 microscope using Texas Red (586 nm excitation/603 nm emission) and GFP (488 nm emission/510 nm excitation) channels.

Evaluating Phosphorylation of β-Catenin. To assess antibody effects on downstream Wnt activation, 3×10^5 MDA-MB-231 cells were seeded per well of a 48-well plate in DMEM medium and incubated overnight. Cells were then treated with PEG−NPs, low FZD7−NPs, or high FZD7−NPs containing no DOX at an equivalent dosage of 5 μM DOX based on matching the number of empty NPs to the corresponding number of DOX-loaded NPs for 24 h. After 24 h, the media/treatments were removed, and the wells were washed twice with PBS before adding trypsin−EDTA to detach the cells. The cells were washed twice with PBS by centrifuging for 5 min at 300 rcf and 21 °C. Cells were fixed with 4% formaldehyde for 10 min and then washed twice with 1X BD Perm/Wash (BD Biosciences). The cells were resuspended in 100 μL of 1X BD Perm/Wash containing 1:500 phospho β-catenin primary antibody (9561S, Cell Signaling Technologies) and incubated for 30 min at room temperature. After incubation, cells were washed twice with 1X BD Perm/Wash. The cells were then resuspended in 100 μL of 1X BD Perm/Wash containing 1:1000 goat antirabbit IgG secondary antibody conjugated with Alexa Fluor 488 (A-11034, ThermoFisher) and incubated for 30 min at room temperature covered from light. Cell samples were washed twice with PBS to remove any unbound antibodies and were resuspended in fresh PBS. Samples were analyzed immediately using flow cytometry. An Acea NovoCyte 2060 Flow Cytometer was used to analyze the FITC channel. Data analysis was performed with NovoExpress software. Density plots showing forward and side scatter data were used to create a primary gate for cells, excluding debris. These experiments were performed in triplicate and analyzed by one-way ANOVA with post hoc Tukey.

RESULTS AND DISCUSSION

Characterization of FZD7-Modified, DOX-Loaded NPs. DOX-loaded PLGA NPs were synthesized and modified with mPEG-SH alone (PEG−DOX−NPs) or in combination with low or high densities of thiolated *anti*-FZD7 antibodies (low FZD7−DOX−NPs and high FZD7−DOX−NPs) as described in the Experimental Section and depicted in Figure 1A. The antibody loading density was tuned by adjusting the initial amount of FZD7-SH added to the DOX-loaded PLGA NPs from 10 μg of FZD7-SH/mg of PLGA for the "low" condition to 30 μg of FZD7-SH/mg of PLGA for the "high" condition. The resulting NPs were characterized using NTA, DLS, and TEM. Prior to surface modification, DOX−NPs had a diameter of 138.8 ± 15.1 nm and a ζ-potential of −9.5 ± 0.5 mV (Figure 1B). Following surface modification, PEG−DOX−NPs had a diameter of 144.5 ± 13.9 nm and a ζ-potential of −15.4 ± 5.0 mV, while the low FZD7−DOX−NPs and the high FZD7−DOX−NPs had diameters of 144.7 ± 14.3 and 146.6 ± 14.9 nm, respectively, and ζ-potentials of −18.8 ± 5.9 and −18.9 ± 7.8 mV, respectively. TEM images indicate that the NPs are spherical and relatively uniform in size (Figure 1C). Additionally, each NP group maintained a stable diameter when suspended in 10% FBS over a 72 h time frame (Figure S2).

DOX encapsulation efficiency (EE%) and loading content (μg DOX/mg PLGA) were quantified by breaking down the DOX−NPs in DMSO and measuring the fluorescence at 480 nm excitation/590 nm emission compared to a standard curve of known DOX concentration in DMSO (Figure 2A). Bare

A

NP Type	μg DOX/mg PLGA	FZD7 antibodies/NP
DOX-NP	13.8 ± 0.9	n/a
PEG-DOX-NP	9.8 ± 1.4	n/a
Low FZD7-DOX-NP	10.3 ± 1.8	348 ± 214
High FZD7-DOX-NP	9.6 ± 1.0	995 ± 197

B

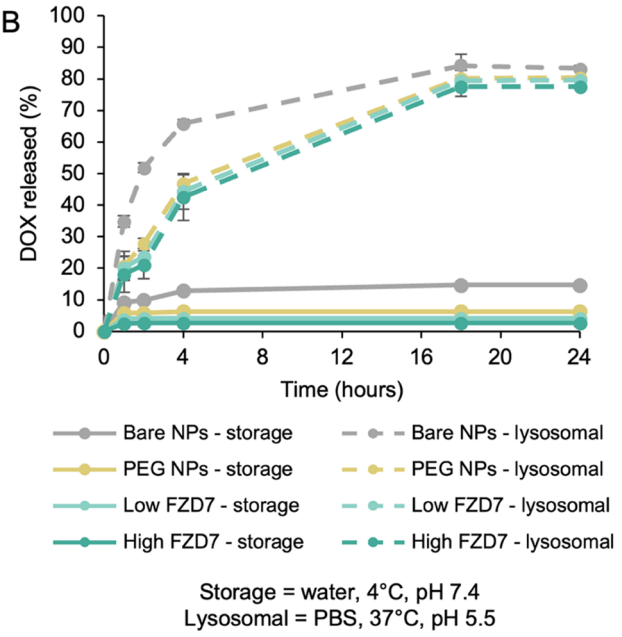

Figure 2. NP cargo loading and drug release kinetics. (A) Loading of DOX in unmodified (bare) DOX−NPs (n = 13), PEG−DOX−NPs (n = 9), low FZD7−DOX−NPs (n = 6), and high FZD7−DOX−NPs (n = 6). Loading of FZD7 as quantified using ELISA on low FZD7−DOX−NPs and high FZD7−DOX−NPs (n = 3). (B) Release of DOX over 24 h from unmodified (bare) DOX−NPs, PEG−DOX−NPs, low FZD7−DOX−NPs, and high FZD7−DOX−NPs in either a storage condition (pH 7.4 water, 4 °C) or a tumor lysosomal condition (pH 5.5 PBS, 37 °C, 100 rpm) (n = 3).

DOX−NPs encapsulated ∼27% of DOX added during synthesis, yielding ∼14 μg of DOX/mg PLGA. Following surface modification, the PEG−DOX−NPs, low FZD7−DOX−NPs, and high FZD7−DOX−NPs all had loading of ∼10 μg of DOX/mg PLGA. Approximately 30% of the DOX cargo was lost postsurface modification, which can likely be attributed to the agitated incubation during the conjugation step as well as the additional wash steps, which may have removed surface-adsorbed DOX. ELISA quantification of FZD7 antibodies on the DOX−NP surface showed ∼30 and ∼90% surface coverages for the "low" and "high" loading conditions, assuming an antibody cross-sectional area of ∼60 nm^2, indicating tunable antibody loading. This surface coverage corresponds to approximately 348 antibodies per

https://doi.org/10.1021/acsomega.3c10275
ACS Omega 2024, 9, 14323−14335

NP and 995 antibodies per NP for the low and high loading conditions, respectively (Figure 2A). To put this in context, theoretical loading was analyzed through quantification of the available maleimide binding sites on the NP surface. This analysis yielded ∼30,000 maleimide groups/NP, which correlates to maleimide to protein ratios of 25:1 and 8:1 for the low and high loading conditions, respectively. The maleimide to protein ratio often ranges from 2:1 up to 25:1 for optimal maleimide−thiol conjugation, confirming that the achieved loading is within a reasonable range based on theoretical calculations.[52]

DOX release from the NPs was assessed by incubating the NPs in either representative storage (pH 7.4 water at 4 °C) or tumor lysosomal (pH 5.5 PBS on a 37 °C shaker) conditions (Figure 2B). The more acidic condition at pH 5.5 is representative of the tumor cell lysosome environment where the NPs should start to break down and release their DOX cargo.[40,41] The release curves indicate minimal (<15%) DOX release from all NPs in the storage condition over 24 h, with a <5% release from the antibody-modified NPs and a faster release from all NPs in the tumor condition. The faster release in the acidic tumor condition is to be expected due to the more rapid degradation of PLGA at lower pH. In the tumor condition, DOX released fastest during the first 4 h of incubation and then released more slowly before plateauing at an ∼80% DOX cargo release at 24 h. Each of the surface-modified NPs exhibited slower DOX release than unmodified NPs in both storage and tumor conditions, indicating that surface modification may provide additional stability to the NPs to prolong breakdown of the polymer.

DOX Delivered via NPs Maintains Its Ability to Localize to the Nucleus and Induce DNA Double Strand Breaks. Since DOX must reach the nucleus to cause DNA double strand breaks, we quantified nuclear levels of DOX and DNA damage in MDA-MB-231 cells exposed to DOX freely or encapsulated in NPs. DOX in the nucleus was analyzed via fluorescence microscopy and quantified using ImageJ. MDA-MB-231 TNBC cells were treated with 5 μM freely delivered DOX, PEG−DOX−NPs, low FZD7−DOX−NPs, or high FZD7−DOX−NPs for 4 or 24 h. Quantification of nuclear DOX indicated slower nuclear localization of DOX when encapsulated in NPs compared to when it is freely delivered (Figure 3A). Levels of antibody conjugation do not seem to affect nuclear DOX delivery. We believe the lack of difference between the targeted and PEGylated NPs is due to similar rates of release of DOX from each NP group. The levels of nuclear DOX observed at 4 h versus 24 h for the NP groups correspond well with the observed kinetics of drug release seen in Figure 2, where ∼45% of the drug was released at 4 h compared to ∼80% at 24 h. Notably, at 24 h, there is no significant difference in nuclear DOX fluorescence for the NPs compared to that in free DOX, indicating that DOX delivered via NPs maintains its ability to localize to the nucleus.

To confirm the delivered DOX retains its mechanism of action, DNA double strand breaks were analyzed by staining for the phosphorylated histone H2A.X at serine 139 using an FITC-conjugated antiphospho H2A.X antibody and then quantified using flow cytometry. This analysis of DNA double strand breaks indicates no significant differences in levels of DNA damage when comparing the freely delivered drug to the encapsulated drug (Figure 3B). Each of the DOX-treated groups had significantly higher levels of DNA double strand break compared to the no-treatment control group. These

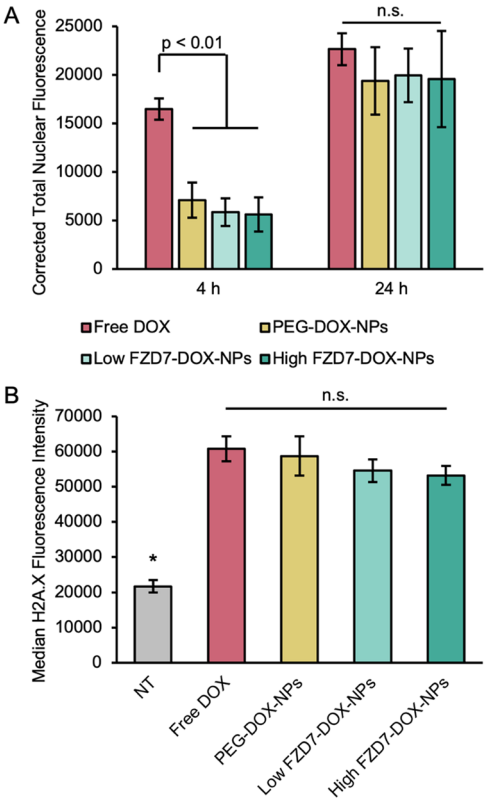

Figure 3. MDA-MB-231 nuclear DOX colocalization and DNA damage. (A) Quantification of the corrected total nuclear fluorescence of DOX from images analyzed in ImageJ (n = 3). Statistical differences were calculated by one-way ANOVA with post hoc Tukey. "n.s." indicates no significant difference between groups at the 95% confidence level. (B) Flow cytometric analysis of cells treated for 24 h with 5 μM DOX and stained with FITC-conjugated phospho-histone H2A.X antibodies (n = 3). Fluorescent labeling is indicative of H2A.X phosphorylation at serine 139 and its corresponding levels of DNA damage. * p < 0.05 versus all other groups as calculated by one-way ANOVA with post hoc Tukey.

results indicate that the encapsulated DOX delivered via PEG-coated or antibody-coated NPs retains its molecular mechanism of action in the nucleus to the same extent as freely delivered DOX.

DOX−NPs Inhibit Cell Function to a Greater Extent than Free DOX. After confirming that DOX delivered via NPs can reach the nucleus to damage DNA, we next investigated the overall effects on cell functioning. Metabolic activity was analyzed in MDA-MB-231 cells using an MTT assay after 24 h of treatment with either 2.5, 5, or 10 μM doses of either free DOX or DOX in NPs (Figure 4A). At each dosage, all three DOX−NPs outperformed the freely delivered DOX with both FZD7−DOX−NP groups, causing significantly greater levels of inhibition at the 5 μM dose. At the 5 μM dose, there was ∼33% inhibition of metabolic activity when cells were treated with freely delivered DOX compared to ∼52 and ∼57% inhibitions for treatment with the low and high FZD7−DOX−NPs, respectively. PEG−DOX−NPs demonstrated an ∼47% inhibition at the 5 μM dose. At the 10 μM dose, each NP treatment caused significantly greater inhibition than the freely delivered DOX with the high FZD7−DOX−NP treatment, showing the most significantly reduced levels of inhibition. The 10 μM dose of freely delivered DOX led to ∼40% inhibition of metabolic activity, while the PEG−DOX−NPs, low FZD7−

https://doi.org/10.1021/acsomega.3c10275
ACS Omega 2024, 9, 14323−14335

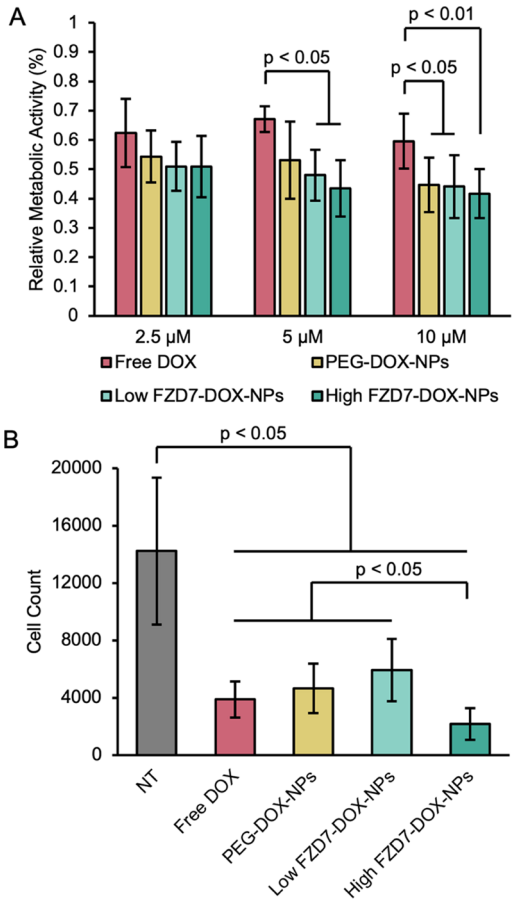

Figure 4. Functional effects of DOX−NPs on MDA-MB-231 cells. (A) Relative metabolic activity of MDA-MB-231 cells after 24 h treatment with either 2.5, 5, or 10 μM of DOX delivered freely (n = 10 for all concentrations) or in NPs (n = 4 for 2.5 μM, n = 5 for 5 and 10 μM) when normalized to a no-treatment control as quantified using an MTT assay. (B) Cell counts of MDA-MB-231 cells after 18 h treatment with 5 μM of DOX either freely delivered or encapsulated in NPs (n = 4). Cell counts were quantified by using flow cytometry after gating to exclude debris. Significance calculated by one-way ANOVA with post hoc Tukey.

DOX−NPs, and high FZD7−DOX−-NPs demonstrated inhibition levels of 55, 56, and 58%, respectively. Overall, DOX when delivered via NPs showed the greatest levels of metabolic activity inhibition, possibly due to the slower release kinetics/nuclear localization lending to a more sustained therapeutic effect.

In addition to metabolic activity, cell counts following treatment with free DOX or DOX-loaded NPs were investigated to further quantify the effects on cell viability. Following treatment for 18 h with a 5 μM dose of either free DOX, PEG−DOX−NPs, low FZD7−DOX−NPs, or high FZD7−DOX−NPs, cells were collected and quantified using flow cytometry (Figure 4B). After the primary gate was created to exclude debris from the cell population, overall cell counts were recorded. Each of the DOX-treated groups, no matter the DOX delivery mechanism, had a significantly smaller cell population compared to the no-treatment control. The high FZD7−DOX−NP treatment group yielded the largest reduction in cell count with a significantly smaller cell population compared with the free DOX, PEG−DOX−NP, and low FZD7−DOX−NP treatments.

To further investigate the effects of each treatment, MDA-MB-231 cells were analyzed for viability, apoptosis, and necrosis. Stages of cell death or viability were identified and quantified through staining with Annexin V and SYTOX AADvanced Dead Cell stain in which MDA-MB-231 cells were treated with 5 μM either free DOX or DOX in NPs for 18 h prior to staining. Samples treated with free DOX showed the greatest levels of apoptotic cells when compared to the control and other treatment groups, with most of the cells in early apoptosis (Figure 5A,B). However, the high FZD7−DOX−NP treatment group had a significantly greater number of cells in the late apoptotic and necrotic stages, indicating that this cell population was further along in the death cycle (Figure 5A,B). Live/Dead staining was also performed on MDA-MB-231 cells that had been treated with 5 μM either free DOX or DOX in NPs for 24 h prior to staining (Figure 5C). Fluorescence microscopy was performed, and representative images indicate cell death in red and live cells in green. All treatment groups showed greater cell death than control, untreated cells. Together, these assays demonstrate that DOX delivered via NPs can reduce cell metabolic activity and number while triggering apoptosis and death. Additionally, they indicate promising effects of including FZD7 antibodies in the formulation, particularly when considering the impact on metabolic activity and cell viability.

FZD7-Targeted NPs Increase β-Catenin Phosphorylation. To analyze any effects of the NPs on Wnt signaling due to the inclusion of *anti*-FZD7 antibodies in the platform, we performed immunofluorescent staining for phosphorylated β-catenin in cells after treatment with empty NPs containing no DOX. The presence of phosphorylated β-catenin suggests increased levels of β-catenin degradation, which would lead to downregulation of the Wnt signal pathway and the subsequent inhibition of Wnt-related oncogenic properties, including drug resistance. The NPs used for this study were synthesized in the same manner as the DOX−NPs without including the DOX cargo in the initial aqueous phase. The mPEG-SH and FZD7-SH conjugation steps remained the same. Following treatment for 24 h, the cells were removed from the plate, stained using an antiphosphorylated β-catenin antibody followed by an FITC-conjugated secondary antibody, and quantified for FITC signal using flow cytometry. Quantification of the FITC signal indicated a higher level of phosphorylated β-catenin in cells treated with both the low and high FZD7−NPs when compared to the no-treatment and PEG−NP control groups. The high FZD7−NPs led to statistically significantly greater levels of phosphorylated β-catenin with almost double the fluorescence intensity than the control nontreated and PEG−NP groups. These higher levels of phosphorylated β-catenin indicate inhibition of the Wnt pathway due to the FZD7 targeting, which supports the earlier analyses in Figure 4 that demonstrated greater effects on cell metabolic activity and viability when treated with the FZD7-targeted NPs.

CONCLUSIONS

In this study, we developed FZD7-targeted polymer NPs capable of delivering chemotherapeutic DOX to MDA-MB-231 TNBC cells in vitro. DOX-loaded NPs surface-modified with *anti*-FZD7 antibodies were successfully synthesized and demonstrated stable cargo retention in storage conditions and sustained drug release in acidic conditions imitating tumor cell lysosomes (Figures 1 and 2). This pH-dependent response is expected from PLGA-based NPs as the polymer breaks down

https://doi.org/10.1021/acsomega.3c10275
ACS Omega 2024, 9, 14323−14335

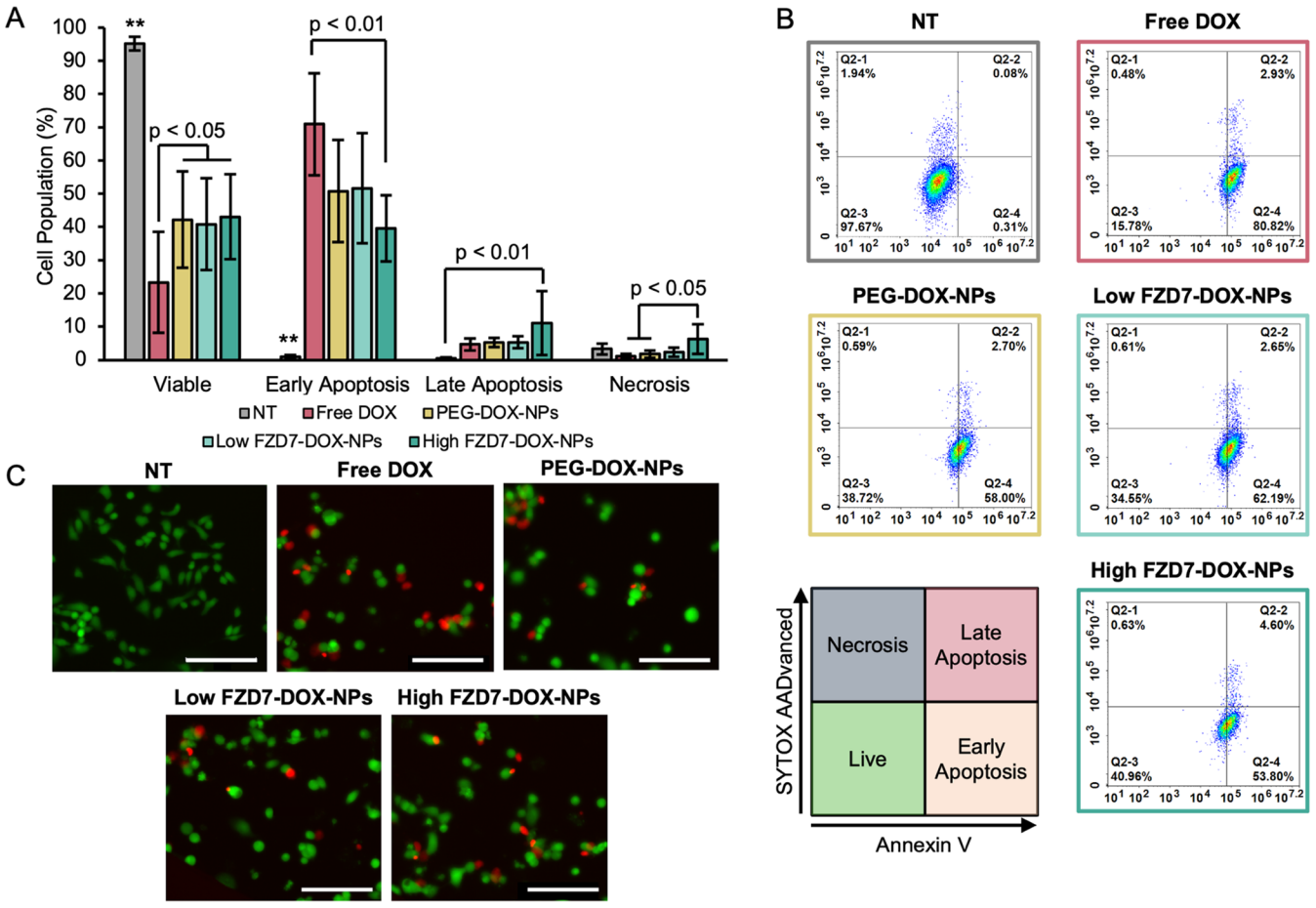

Figure 5. Analysis of apoptosis and death in MDA-MB-231 cells following treatment with DOX delivered freely or in NPs. (A) Flow cytometry analysis of cells 18 h post treatment with 5 μM freely delivered DOX or DOX in NPs ($n = 5$). ** $p < 0.001$ versus all other groups as calculated by one-way ANOVA with post hoc Tukey. (B) Representative scatterplots demonstrating the fraction of cells in early apoptosis (bottom right quadrant), late apoptosis (top right quadrant), or necrosis (top left quadrant). (C) Representative Live/Dead images of cells after 24 h treatment with 5 μM of freely delivered DOX or DOX in NPs. Red fluorescence indicates dead cells, and green fluorescence indicates live cells. Scale bars = 150 μm.

into lactic and glycolic acids.[53,54] Additionally, water uptake into the NP leads to the production of acidic oligomers, which creates an acidic environment inside the NP and accelerates the degradation.[55] This rate of degradation can be adjusted based on the size and porosity of the NP.[56,57] We showed that DOX encapsulation in NPs did not hinder its ability to colocalize with the nucleus to the same degree as freely delivered DOX over a 24 h period (Figure 3A). Furthermore, DOX maintained its molecular mechanism of action in the nucleus, as seen through similar levels of H2A.X phosphorylation, indicative of DNA double strand breakages and its corresponding DNA damage (Figure 3B). After 24 h of treatment at three different dosage concentrations, all three DOX−NPs outperformed the freely delivered DOX in inhibiting metabolic activity (Figure 4A). This is in agreement with previous studies comparing the efficacy of freely delivered DOX to NP-mediated delivery of DOX.[17,58] The low and high FZD7−DOX−NPs, respectively, caused ∼20 and ∼25% greater inhibitions of metabolic activity at the 5 μM dose when compared to the freely delivered DOX. In agreement with these results, DOX-treated cells all had significantly smaller cell populations than untreated cells, with the high FZD7−DOX−NP treatment yielding the largest reduction of cell number (Figure 4B). When the mechanism of cell death was investigated, the freely delivered DOX led to the highest levels of overall apoptosis; however, the high FZD7−DOX−NPs demonstrated the largest population in the late apoptosis stage (Figure 5). Finally, analysis of phosphorylated β-catenin confirmed that including FZD7 antibodies in the NP design yielded the suppression of Wnt signaling (Figure 6), which may explain why the FZD7−DOX−NPs, particularly those with a high antibody loading, were more potent than PEG−DOX−NPs in terms of suppressing metabolic activity and cell count. Overall, these results indicate great potential for an FZD7-targeted delivery system to improve the potency of DOX chemotherapy in TNBC and support the continued investigation of Wnt suppression to enhance TNBC therapies more generally.

While results from metabolic activity, overall cell population, and β-catenin phosphorylation assays show some benefit to the FZD7 targeting, the improvement was relatively modest. This may be because in vitro experiments cannot recapitulate the complex interactions between NPs and biological systems observed in vivo. Alternatively, it could be that the NP design requires further optimization to maximize the targeting potency compared to free DOX or nontargeted PEG−DOX−NPs. To further investigate how FZD7 targeting improves therapeutic efficacy of drugs such as DOX, NP

https://doi.org/10.1021/acsomega.3c10275
ACS Omega 2024, 9, 14323−14335

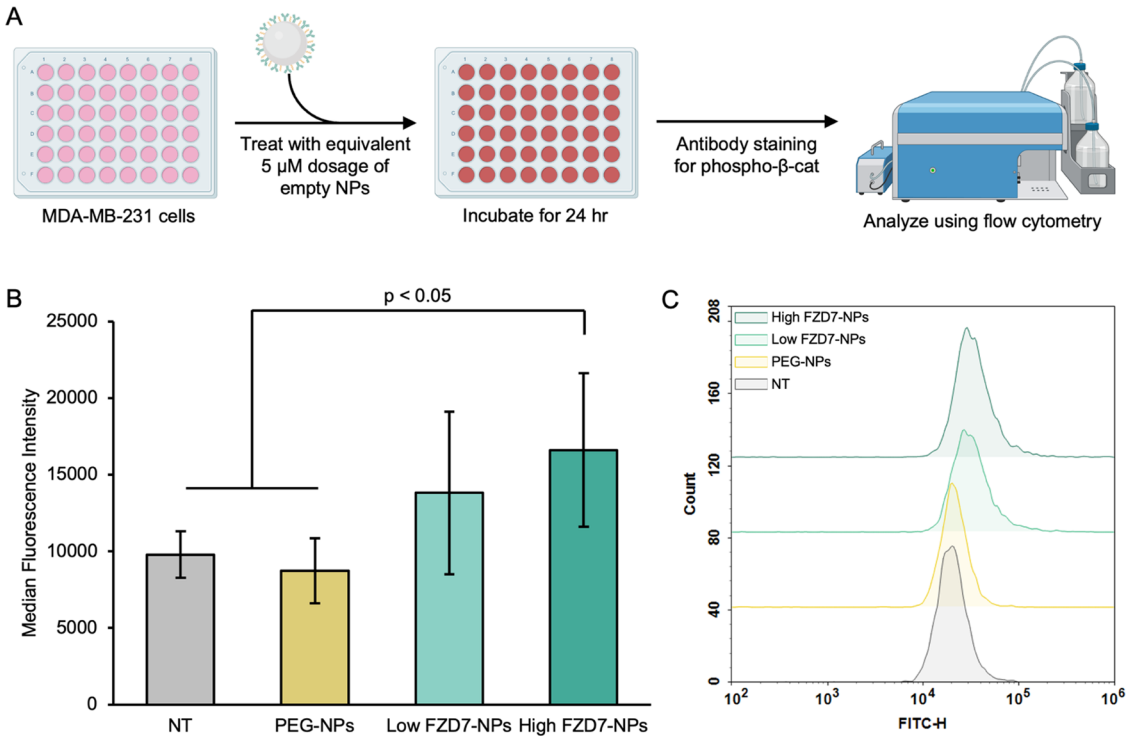

Figure 6. Effects of FZD7 targeting on β-catenin phosphorylation. (A) Scheme of the experimental procedure to assess the effects of empty FZD7 antibody-conjugated NPs on β-catenin phosphorylation in MDA-MB-231 cells. Created with BioRender.com. (B) Quantification of phosphorylated β-catenin via an FITC-conjugated secondary antibody using flow cytometry. Background signal due to nonspecific binding of the secondary antibody was subtracted from the reported values (n = 3). Significance calculated by one-way ANOVA with post hoc Tukey. (C) Representative flow cytometry histogram of FITC-stained phosphorylated β-catenin signal in each treatment group.

interactions with the cell and more specifically the mechanism of uptake and internalization could be assessed. This analysis would provide insight into which pathways lead to higher NP uptake and retention, which can be taken advantage of when designing future iterations of this platform. One possible change would be to adjust the antibody conjugation mechanism by using a linker; extending the antibodies outward from the NP surface could improve interactions with cell membrane receptors, leading to more efficient binding with target cells. Furthermore, tuning of the NP structure itself such as changes to the polymer concentration, molecular weight, or PEG content could adjust properties such as drug release and NP degradation. This optimization could improve drug delivery to the cells by allowing adequate time for the NPs to circulate when the system is introduced to an in vivo environment.

Future studies to expand on this work could transition to in vivo experiments to clarify the impact of FZD7 antibody loading density on the ability of the NPs to target TNBC tumors at different stages of development, which may exhibit higher or lower levels of FZD7 expression along with having different degrees of vascularization. While high FZD7−DOX−NPs tended to outperform the low FZD7−DOX−NPs and the PEG−DOX−NPs in the in vitro studies performed here, the differences between groups will also need to be evaluated in vivo. In addition to assessing the impact of each treatment on primary tumor growth, the effects on recurrence and metastasis could also be evaluated, as this would provide valuable information regarding the ability of combined FZD7 targeting/Wnt inhibition and DOX delivery to limit TNBC progression. As part of this work, dosing optimization will need to be performed along with pharmacokinetic analyses to determine drug clearance over time and drug accumulation in tumors versus off-target tissues. Finally, since toxicity is a major concern for DOX that limits its clinical use, future studies should evaluate the toxicity of each formulation as compared to free DOX and/or Doxil, as demonstrating reduced toxicity would be valuable.

In conclusion, the targeting of FZD7 receptors is a promising approach to more specifically and effectively treat TNBC. In this study, the DOX-loaded, *anti*-FZD7 antibody-modified NPs effectively delivered their cargo to TNBC cells, triggered Wnt inhibition, as evidenced by increased β-catenin phosphorylation, and led to greater inhibition of cell functionality. With further investigation, these NPs or iterations of this design may lead to a more effective or safer targeted chemotherapy regimen for TNBC.

■ ASSOCIATED CONTENT

Supporting Information

The Supporting Information is available free of charge at https://pubs.acs.org/doi/10.1021/acsomega.3c10275.

DOX loading capacity and encapsulation efficiency as a function of the initial amount of DOX added during NP synthesis (Figure S1); diameter stability of NPs in serum condition (Figure S2); representative images for DOX nuclear colocalization (Figure S3); demonstration of nuclear DOX quantification method (Figure S4), and relative metabolic activity of MDA-MB-231 cells treated with increasing doses of free DOX or with increasing doses of empty PLGA NPs (Figure S5) (PDF)

https://doi.org/10.1021/acsomega.3c10275
ACS Omega 2024, 9, 14323−14335

AUTHOR INFORMATION

Corresponding Author

Emily S. Day − *Department of Biomedical Engineering, University of Delaware, Newark, Delaware 19713, United States; Department of Materials Science and Engineering, University of Delaware, Newark, Delaware 19716, United States; Helen F. Graham Cancer Center and Research Institute, Newark, Delaware 19713, United States;* orcid.org/0000-0002-8707-826X; Email: emilyday@udel.edu

Authors

Elise C. Hoover − *Department of Biomedical Engineering, University of Delaware, Newark, Delaware 19713, United States;* orcid.org/0000-0003-4723-7446

Olivia M. Ruggiero − *Department of Biomedical Engineering, University of Delaware, Newark, Delaware 19713, United States;* Present Address: United States Patent & Trademark Office (USPTO), 600 Dulany St, Alexandria, Virginia 22314, United States

Rachel N. Swingler − *Department of Biomedical Engineering, University of Delaware, Newark, Delaware 19713, United States;* Present Address: Cartesian Therapeutics, 704 Quince Orchard Rd, Ste. 210, Gaithersburg, Maryland 20878, United States.

Complete contact information is available at: https://pubs.acs.org/10.1021/acsomega.3c10275

Author Contributions

The manuscript was written through contributions of all authors. All authors have given approval to the final version of the manuscript.

Funding

This project was supported by the National Institutes of Health (NIH) under award number R01CA211925 as well as the University of Delaware Graduate College University Doctoral Fellowship for Excellence. O.M.R. acknowledges support from the University of Delaware Summer Scholars Program.

Notes

The authors declare no competing financial interest.

ACKNOWLEDGMENTS

The authors thank Shannon Modla of the Delaware Bioimaging Center for assistance with TEM sample preparation and imaging of nanoparticles.

ABBREVIATIONS

TNBC, triple-negative breast cancer; HER2, human epidermal growth factor receptor 2; DOX, doxorubicin; NPs, nanoparticles; FZD7, Frizzled7; MDR1, multidrug-resistant protein-1; PLGA−PEG−MAL, poly(lactide-*co*-glycolide)−polyethylene glycol−maleimide; DCM, dichloromethane; PVA, poly(vinyl alcohol); MWCO, molecular weight cutoff; (EDTA), ethylenediaminetetraacetic acid; TCEP, tris(2-carboxyethyl) phosphine hydrochloride; NTA, nanoparticle tracking analysis; TEM, transmission electron microscope; ELISA, enzyme-linked immunosorbent assay; HRP, horseradish peroxidase; TMB, 3,3′,5,5′-tetramethylbenzidine; DMSO, dimethyl sulfoxide; EE%, encapsulation efficiency; LC, loading capacity; FBS, fetal bovine serum; CTNF, corrected total nuclear fluorescence

REFERENCES

(1) CDCBreastCancer. Breast Cancer Statistics. Centers for Disease Control and Prevention. 2023 https://www.cdc.gov/cancer/breast/statistics/index.htm. (accessed September 14, 2023).

(2) American Cancer Society. Breast Cancer Facts & Figures. 2017, pp 2017−2018.

(3) Bauer, K. R.; Brown, M.; Cress, R. D.; Parise, C. A.; Caggiano, V. Descriptive Analysis of Estrogen Receptor (ER)-Negative, Progesterone Receptor (PR)-Negative, and HER2-Negative Invasive Breast Cancer, the so-Called Triple-Negative Phenotype. *Cancer* **2007**, *109* (9), 1721−1728.

(4) Hsu, J.-Y.; Chang, C.-J.; Cheng, J.-S. Survival, Treatment Regimens and Medical Costs of Women Newly Diagnosed with Metastatic Triple-Negative Breast Cancer. *Sci. Rep.* **2022**, *12* (1), No. 729.

(5) Yin, L.; Duan, J.-J.; Bian, X.-W.; Yu, S. Triple-Negative Breast Cancer Molecular Subtyping and Treatment Progress. *Breast Cancer Res.* **2020**, *22* (1), No. 61.

(6) Holleczek, B.; Stegmaier, C.; Radosa, J. C.; Solomayer, E.-F.; Brenner, H. Risk of Loco-Regional Recurrence and Distant Metastases of Patients with Invasive Breast Cancer up to Ten Years after Diagnosis − Results from a Registry-Based Study from Germany. *BMC Cancer* **2019**, *19* (1), No. 520.

(7) Zerdan, M. B.; Ghorayeb, T.; Saliba, F.; Allam, S.; Zerdan, M. B.; Yaghi, M.; Bilani, N.; Jaafar, R.; Nahleh, Z. Triple Negative Breast Cancer: Updates on Classification and Treatment in 2021. *Cancers* **2022**, *14* (5), No. 1253.

(8) Chang-Qing, Y.; Jie, L.; Shi-Qi, Z.; Kun, Z.; Zi-Qian, G.; Ran, X.; Hui-Meng, L.; Ren-Bin, Z.; Gang, Z.; Da-Chuan, Y.; Chen-Yan, Z. Recent Treatment Progress of Triple Negative Breast Cancer. *Prog. Biophys. Mol. Biol.* **2020**, *151*, 40−53.

(9) Mandapati, A.; Lukong, K. E. Triple Negative Breast Cancer: Approved Treatment Options and Their Mechanisms of Action. *J. Cancer Res. Clin. Oncol.* **2023**, *149* (7), 3701−3719.

(10) Medina, M. A.; Oza, G.; Sharma, A.; Arriaga, L. G.; Hernández, J. M. H.; Rotello, V. M.; Ramirez, J. T. Triple-Negative Breast Cancer: A Review of Conventional and Advanced Therapeutic Strategies. *Int. J. Environ. Res. Public Health* **2020**, *17* (6), No. 2078.

(11) Mansoori, B.; Mohammadi, A.; Jang, S. S.; Baradaran, B. Mechanisms of Immune System Activation in Mammalians by Small Interfering RNA (siRNA). *Artif. Cells, Nanomed., Biotechnol.* **2016**, *44* (7), 1589−1596.

(12) van der Zanden, S. Y.; Qiao, X.; Neefjes, J. New Insights into the Activities and Toxicities of the Old Anticancer Drug Doxorubicin. *FEBS J.* **2021**, *288* (21), 6095−6111.

(13) Dulf, P. L.; Mocan, M.; Coadă, C. A.; Dulf, D. V.; Moldovan, R.; Baldea, I.; Farcas, A.-D.; Blendea, D.; Filip, A. G. Doxorubicin-Induced Acute Cardiotoxicity Is Associated with Increased Oxidative Stress, Autophagy, and Inflammation in a Murine Model. *Naunyn-Schmiedeberg's Arch. Pharmacol.* **2023**, *396* (6), 1105−1115.

(14) Cai, F.; Luis, M. A. F.; Lin, X.; Wang, M.; Cai, L.; Cen, C.; Biskup, E. Anthracycline-induced Cardiotoxicity in the Chemotherapy Treatment of Breast Cancer: Preventive Strategies and Treatment (Review). *Mol. Clin. Oncol.* **2019**, *11* (1), 15−23.

(15) Janes, K. A.; Fresneau, M. P.; Marazuela, A.; Fabra, A.; Alonso, M. J. Chitosan Nanoparticles as Delivery Systems for Doxorubicin. *J. Controlled Release* **2001**, *73* (2), 255−267.

(16) Harris, J. C.; Sterin, E. H.; Day, E. S. Membrane-Wrapped Nanoparticles for Enhanced Chemotherapy of Acute Myeloid Leukemia. *ACS Biomater. Sci. Eng.* **2022**, *8* (10), 4439−4448.

(17) Gabizon, A.; Catane, R.; Uziely, B.; Kaufman, B.; Safra, T.; Cohen, R.; Martin, F.; Huang, A.; Barenholz, Y. Prolonged Circulation Time and Enhanced Accumulation in Malignant Exudates of Doxorubicin Encapsulated in Polyethylene-Glycol Coated Liposomes1. *Cancer Res.* **1994**, *54* (4), 987−992.

(18) Ball, R. L.; Bajaj, P.; Whitehead, K. A. Achieving Long-Term Stability of Lipid Nanoparticles: Examining the Effect of pH, Temperature, and Lyophilization. *Int. J. Nanomed.* **2017**, *12*, 305−315.

(19) Chen, C.; Han, D.; Cai, C.; Tang, X. An Overview of Liposome Lyophilization and Its Future Potential. *J. Controlled Release* **2010**, *142* (3), 299−311.
(20) Pohl, S.-G.; Brook, N.; Agostino, M.; Arfuso, F.; Kumar, A. P.; Dharmarajan, A. Wnt Signaling in Triple-Negative Breast Cancer. *Oncogenesis* **2017**, *6* (4), e310.
(21) Ganesh, S.; Koser, M. L.; Cyr, W. A.; Chopda, G. R.; Tao, J.; Shui, X.; Ying, B.; Chen, D.; Pandya, P.; Chipumuro, E.; Siddiquee, Z.; Craig, K.; Lai, C.; Dudek, H.; Monga, S. P.; Wang, W.; Brown, B. D.; Abrams, M. T. Direct Pharmacological Inhibition of β-Catenin by RNA Interference in Tumors of Diverse Origin. *Mol. Cancer Ther.* **2016**, *15* (9), 2143−2154.
(22) Acebron, S. P.; Karaulanov, E.; Berger, B. S.; Huang, Y.-L.; Niehrs, C. Mitotic Wnt Signaling Promotes Protein Stabilization and Regulates Cell Size. *Mol. Cell* **2014**, *54* (4), 663−674.
(23) Yang, L.; Wu, X.; Wang, Y.; Zhang, K.; Wu, J.; Yuan, Y.-C.; Deng, X.; Chen, L.; Kim, C. C. H.; Lau, S.; Somlo, G.; Yen, Y. FZD7 Has a Critical Role in Cell Proliferation in Triple Negative Breast Cancer. *Oncogene* **2011**, *30* (43), 4437−4446.
(24) Valcourt, D. M.; Dang, M. N.; Wang, J.; Day, E. S. Nanoparticles for Manipulation of the Developmental Wnt, Hedgehog, and Notch Signaling Pathways in Cancer. *Ann. Biomed. Eng.* **2020**, *48* (7), 1864−1884.
(25) Steward, L. T.; Gao, F.; Taylor, M. A.; Margenthaler, J. A. Impact of Radiation Therapy on Survival in Patients with Triple-Negative Breast Cancer. *Oncol. Lett.* **2014**, *7* (2), 548−552.
(26) Geyer, F. C.; Lacroix-Triki, M.; Savage, K.; Arnedos, M.; Lambros, M. B.; MacKay, A.; Natrajan, R.; Reis-Filho, J. S. β-Catenin Pathway Activation in Breast Cancer Is Associated with Triple-Negative Phenotype but Not with CTNNB1Mutation. *Mod. Pathol.* **2011**, *24* (2), 209−231.
(27) Nguyen, V. H. L.; Hough, R.; Bernaudo, S.; Peng, C. Wnt/β-Catenin Signalling in Ovarian Cancer: Insights into Its Hyperactivation and Function in Tumorigenesis. *J. Ovarian Res.* **2019**, *12* (1), No. 122.
(28) Zhao, H.; Ming, T.; Tang, S.; Ren, S.; Yang, H.; Liu, M.; Tao, Q.; Xu, H. Wnt Signaling in Colorectal Cancer: Pathogenic Role and Therapeutic Target. *Mol. Cancer* **2022**, *21* (1), No. 144.
(29) Xu, X.; Zhang, M.; Xu, F.; Jiang, S. Wnt Signaling in Breast Cancer: Biological Mechanisms, Challenges and Opportunities. *Mol. Cancer* **2020**, *19* (1), No. 165.
(30) Howe, L. R.; Brown, A. M. C. Wnt Signaling and Breast Cancer. *Cancer Biol. Ther.* **2004**, *3* (1), 36−41.
(31) King, T. D.; Zhang, W.; Suto, M. J.; Li, Y. Frizzled7 as an Emerging Target for Cancer Therapy. *Cell. Signalling* **2012**, *24* (4), 846−851.
(32) Gruber, J.; Yee, Z.; Tolwinski, N. S. Developmental Drift and the Role of Wnt Signaling in Aging. *Cancers* **2016**, *8* (8), No. 73.
(33) Clevers, H.; Nusse, R. Wnt/β-Catenin Signaling and Disease. *Cell* **2012**, *149* (6), 1192−1205.
(34) Jho, E.-h.; Zhang, T.; Domon, C.; Joo, C.-K.; Freund, J.-N.; Costantini, F. Wnt/β-Catenin/Tcf Signaling Induces the Transcription of Axin2, a Negative Regulator of the Signaling Pathway. *Mol. Cell. Biol.* **2002**, *22* (4), 1172−1183.
(35) Pelengaris, S.; Khan, M.; Evan, G. C-MYC: More than Just a Matter of Life and Death. *Nat. Rev. Cancer* **2002**, *2* (10), 764−776.
(36) Kafri, P.; Hasenson, S. E.; Kanter, I.; Sheinberger, J.; Kinor, N.; Yunger, S.; Shav-Tal, Y. Quantifying β-Catenin Subcellular Dynamics and Cyclin D1 mRNA Transcription during Wnt Signaling in Single Living Cells. *eLife* **2016**, *5*, No. e16748.
(37) de Sousa E Melo, F.; Colak, S.; Buikhuisen, J.; Koster, J.; Cameron, K.; de Jong, J. H.; Tuynman, J. B.; Prasetyanti, P. R.; Fessler, E.; van den Bergh, S. P.; Rodermond, H.; Dekker, E.; van der Loos, C. M.; Pals, S. T.; van de Vijver, M. J.; Versteeg, R.; Richel, D. J.; Vermeulen, L.; Medema, J. P. Methylation of Cancer-Stem-Cell-Associated Wnt Target Genes Predicts Poor Prognosis in Colorectal Cancer Patients. *Cell Stem Cell* **2011**, *9* (5), 476−485.
(38) Do, M.; Wu, C. C. N.; Sonavane, P. R.; Juarez, E. F.; Adams, S. R.; Ross, J.; Baena, A. R. y.; Patel, C.; Mesirov, J. P.; Carson, D. A.; Advani, S. J.; Willert, K. A FZD7-Specific Antibody−Drug Conjugate Induces Ovarian Tumor Regression in Preclinical Models. *Mol. Cancer Ther.* **2022**, *21* (1), 113−124.
(39) Riley, R. S.; Day, E. S. Frizzled7 Antibody-Functionalized Nanoshells Enable Multivalent Binding for Wnt Signaling Inhibition in Triple Negative Breast Cancer Cells. *Small* **2017**, *13* (26), No. 1700544.
(40) Wang, J.; Dang, M. N.; Day, E. S. Inhibition of Wnt Signaling by Frizzled7 Antibody-Coated Nanoshells Sensitizes Triple-Negative Breast Cancer Cells to the Autophagy Regulator Chloroquine. *Nano Res.* **2020**, *13* (6), 1693−1703.
(41) Pode-Shakked, N.; Harari-Steinberg, O.; Haberman-Ziv, Y.; Rom-Gross, E.; Bahar, S.; Omer, D.; Metsuyanim, S.; Buzhor, E.; Jacob-Hirsch, J.; Goldstein, R. S.; Mark-Danieli, M.; Dekel, B. Resistance or Sensitivity of Wilms' Tumor to Anti-FZD7 Antibody Highlights the Wnt Pathway as a Possible Therapeutic Target. *Oncogene* **2011**, *30* (14), 1664−1680.
(42) Merikhian, P.; Eisavand, M. R.; Farahmand, L. Triple-Negative Breast Cancer: Understanding Wnt Signaling in Drug Resistance. *Cancer Cell Int.* **2021**, *21* (1), No. 419.
(43) Cui, C.; Zhou, X.; Zhang, W.; Qu, Y.; Ke, X. Is β-Catenin a Druggable Target for Cancer Therapy? *Trends Biochem. Sci.* **2018**, *43* (8), 623−634.
(44) Makhani, E. Y.; Zhang, A.; Haun, J. B. Quantifying and Controlling Bond Multivalency for Advanced Nanoparticle Targeting to Cells. *Nano Convergence* **2021**, *8* (1), No. 38.
(45) Liu, J.; Toy, R.; Vantucci, C.; Pradhan, P.; Zhang, Z.; Kuo, K. M.; Kubelick, K. P.; Huo, D.; Wen, J.; Kim, J.; Lyu, Z.; Dhal, S.; Atalis, A.; Ghosh-Choudhary, S. K.; Devereaux, E. J.; Gumbart, J. C.; Xia, Y.; Emelianov, S. Y.; Willett, N. J.; Roy, K. Bifunctional Janus Particles as Multivalent Synthetic Nanoparticle Antibodies (SNAbs) for Selective Depletion of Target Cells. *Nano Lett.* **2021**, *21* (1), 875−886.
(46) Woythe, L.; Tito, N. B.; Albertazzi, L. A Quantitative View on Multivalent Nanomedicine Targeting. *Adv. Drug Delivery Rev.* **2021**, *169*, 1−21.
(47) Valcourt, D. M.; Day, E. S. Dual Regulation of miR-34a and Notch Signaling in Triple-Negative Breast Cancer by Antibody/miRNA Nanocarriers. *Mol. Ther.–Nucleic Acids* **2020**, *21*, 290−298.
(48) Ning, S.-T.; Lee, S.-Y.; Wei, M.-F.; Peng, C.-L.; Lin, S. Y.-F.; Tsai, M.-H.; Lee, P.-C.; Shih, Y.-H.; Lin, C.-Y.; Luo, T.-Y.; Shieh, M.-J. Targeting Colorectal Cancer Stem-Like Cells with Anti-CD133 Antibody-Conjugated SN-38 Nanoparticles. *ACS Appl. Mater. Interfaces* **2016**, *8* (28), 17793−17804.
(49) Johnston, M. C.; Nicoll, J. A.; Redmond, K. M.; Smyth, P.; Greene, M. K.; McDaid, W. J.; Chan, D. K. W.; Crawford, N.; Stott, K. J.; Fox, J. P.; Straubinger, N. L.; Roche, S.; Clynes, M.; Straubinger, R. M.; Longley, D. B.; Scott, C. J. DR5-Targeted, Chemotherapeutic Drug-Loaded Nanoparticles Induce Apoptosis and Tumor Regression in Pancreatic Cancer in Vivo Models. *J. Controlled Release* **2020**, *324*, 610−619.
(50) Astete, C. E.; Sabliov, C. M. Synthesis and Characterization of PLGA Nanoparticles. *J. Biomater. Sci., Polym. Ed.* **2006**, *17* (3), 247−289.
(51) Si, W.; Yang, Q.; Zong, Y.; Ren, G.; Zhao, L.; Hong, M.; Xin, Z. Toward Understanding the Effect of Solvent Evaporation on the Morphology of PLGA Microspheres by Double Emulsion Method. *Ind. Eng. Chem. Res.* **2021**, *60* (25), 9196−9205.
(52) Martínez-Jothar, L.; Doulkeridou, S.; Schiffelers, R. M.; Torano, J. S.; Oliveira, S.; van Nostrum, C. F.; Hennink, W. E. Insights into Maleimide-Thiol Conjugation Chemistry: Conditions for Efficient Surface Functionalization of Nanoparticles for Receptor Targeting. *J. Controlled Release* **2018**, *282*, 101−109.
(53) Zolnik, B. S.; Burgess, D. J. Effect of Acidic pH on PLGA Microsphere Degradation and Release. *J. Controlled Release* **2007**, *122* (3), 338−344.
(54) Faisant, N.; Siepmann, J.; Benoit, J. P. PLGA-Based Microparticles: Elucidation of Mechanisms and a New, Simple Mathematical Model Quantifying Drug Release. *Eur. J. Pharm. Sci.* **2002**, *15* (4), 355−366.

https://doi.org/10.1021/acsomega.3c10275
ACS Omega 2024, 9, 14323−14335

(55) Fu, K.; Pack, D. W.; Klibanov, A. M.; Langer, R. Visual Evidence of Acidic Environment Within Degrading Poly(Lactic-Co-Glycolic Acid) (PLGA) Microspheres. *Pharm. Res.* **2000**, *17* (1), 100−106.
(56) Keles, H.; Naylor, A.; Clegg, F.; Sammon, C. Investigation of Factors Influencing the Hydrolytic Degradation of Single PLGA Microparticles. *Polym. Degrad. Stab.* **2015**, *119*, 228−241.
(57) Rapier, C. E.; Shea, K. J.; Lee, A. P. Investigating PLGA Microparticle Swelling Behavior Reveals an Interplay of Expansive Intermolecular Forces. *Sci. Rep.* **2021**, *11* (1), No. 14512.
(58) Alibolandi, M.; Abnous, K.; Mohammadi, M.; Hadizadeh, F.; Sadeghi, F.; Taghavi, S.; Jaafari, M. R.; Ramezani, M. Extensive Preclinical Investigation of Polymersomal Formulation of Doxorubicin versus Doxil-Mimic Formulation. *J. Controlled Release* **2017**, *264*, 228−236.

https://doi.org/10.1021/acsomega.3c10275
ACS Omega 2024, 9, 14323−14335